Geochemistry Geophysics Geosystems G3
AN ELECTRONIC JOURNAL OF THE EARTH SCIENCES
Published by AGU and the Geochemical Society

Article
Volume 5, Number 1
17 January 2004
Q01004, doi:10.1029/2003GC000604
ISSN: 1525-2027

Upper crustal seismic velocity structure and microearthquake depths at the Endeavour Segment, Juan de Fuca Ridge

Andrew H. Barclay and William S. D. Wilcock
School of Oceanography, University of Washington, Box 357940, Seattle, Washington 98195, USA (andrew@ocean.washington.edu; wilcock@ocean.washington.edu)

[1] We present the results of a study to invert microearthquake and explosive shot data from the Endeavour segment of the intermediate-spreading Juan de Fuca Ridge. The average isotropic *P* wave velocity structure, derived from the shot data, in the uppermost 1.5 km of the oceanic crust is characterized by an increase with age of ~8% from the axis to at least 0.5 Ma, that is attributed to the sealing of layer 2A porosity by hydrothermal processes. Superimposed on this variation are axis-parallel, 2-km-wide, alternating bands of high and low velocity with a peak-to-peak variation of 5–12%. High and low velocities away from the axis correspond to bathymetric trenches and ridges, respectively and are likely due to variations in layer 2A thickness. *P* wave azimuthal anisotropy is present in the data that is best fit with a model of 9% anisotropy at 750 m depth, decreasing to 1% at 3 km depth and is likely due to the preferential alignment of vertical cracks and fissures in the along-axis direction. Anisotropy and velocity heterogeneity are coupled; anisotropy alone may explain the form but not the magnitude of the axis-parallel bands. There are strong trade-offs between the hypocentral depths of microearthquakes and the *P* and *S* wave velocity structures. Changing the mean hypocentral depth by up to 0.5 km leads to only modest increases in the travel time RMS but the resulting velocity models appear more feasible when the earthquakes are forced deeper than when they are forced shallower.

Components: 11,817 words, 13 figures, 1 table.

Keywords: Mid-ocean ridge; layer 2A structure; seismic anisotropy; microearthquakes.

Index Terms: 3035 Marine Geology and Geophysics: Midocean ridge processes; 7220 Seismology: Oceanic crust.

Received 20 July 2003; **Revised** 10 October 2003; **Accepted** 21 October 2003; **Published** 17 January 2004.

Barclay, A. H., and W. S. D. Wilcock (2004), Upper crustal seismic velocity structure and microearthquake depths at the Endeavour Segment, Juan de Fuca Ridge, *Geochem. Geophys. Geosyst.*, *5*, Q01004, doi:10.1029/2003GC000604.

1. Introduction

[2] Microearthquake studies on mid-ocean ridges have generally been motivated by a desire to constrain the characteristics of faulting and the depth to the brittle-ductile transition. As such they have contributed to our understanding of the importance of tectonism in the accretion of oceanic crust and its variation with spreading rate [e.g., *Riedesel et al.*, 1982; *Toomey et al.*, 1985; *Hildebrand et al.*, 1997]. On slow-spreading ridges, where earthquakes are numerous and can extend to lower crust, microearthquake arrival time data have also been successfully combined with small amounts of refraction data to image seismic structure through the use of joint inversions for seismic velocity and hypocentral parameters [*Toomey et al.*, 1988; *Kong*, 1990; *Barclay et al.*, 2001]. These studies have constrained shear wave velocities and imaged mid- and lower-crustal

low velocity zones that result from thermal anomalies and partial melt.

[3] Studies that have resolved lateral variations in the velocity structure of the upper crust at mid-ocean ridges have placed important constraints on volcanic processes responsible for the formation of young crust and how it varies between slow and fast spreading rates. The fast spreading East Pacific Rise is characterized by a narrow (~2–4 km wide) band of high velocities directly beneath the axis [*Toomey et al.*, 1990, 1994; *Harding et al.*, 1993; *Christeson et al.*, 1996; *Hussenoeder et al.*, 2002]. This feature is restricted to the uppermost ~800 m in tomographic images [*Toomey et al.*, 1994], is continuous along-axis, and has been attributed to the proximity of the sheeted dikes to the surface that subside as they are progressively buried by off-axis emplacement of extrusives [e.g., *Hooft et al.*, 1996]. The shallow velocity structure shows few other features and has little variation in the along-axis direction [*Toomey et al.*, 1994] suggesting that magmatic processes are fairly uniform along axis as evidenced by the presence of a mid-crustal magma lens that is continuous along-axis in many locations [e.g., *Detrick et al.*, 1993].

[4] In contrast, the slow spreading Mid-Atlantic Ridge (MAR) shows a relatively high degree of heterogeneity in both the along- and cross-axis directions that has no along-axis continuity. Instead, the shallow crust at the MAR is characterized by discrete low velocity regions that are spatially associated with seamounts. On the basis of this association, these regions have been attributed to either the higher porosities of a locally thicker extrusive layer or the higher temperatures of the magma plumbing system [*Barclay et al.*, 1998; *Magde et al.*, 2000]. Such observations support models in which volcanic accretion is discontinuous along axis [*Smith and Cann*, 1992].

[5] In this paper, we present the results of a study to invert microearthquake and explosive shot data on an intermediate spreading rate ridge; the Endeavour Segment of the Juan de Fuca Ridge. The microearthquake data set had previously been analyzed for the distribution and characteristics of earthquakes and their tectonic implications [*Wilcock et al.*, 2002] as well as for shear wave splitting [*Almendros et al.*, 2000] and tidal triggering [*Wilcock*, 2001]. Here we present inversions of the shot and earthquake data that constrain the upper crustal velocity structure and its variation with age and the trade-offs between *P* wave velocity structure, V_P/V_S structure, and the depths of axial earthquakes. The results are used to constrain the processes of crustal accretion at an intermediate spreading ridge.

2. Endeavour Segment

[6] The Endeavour segment (Figure 1) lies in a tectonically complex region near the northern end of the Juan de Fuca Ridge. Along the central portion of the segment the spreading axis is defined by a 0.5-km-wide and 0.1-km-deep axial valley that splits a 4-km-wide axial high [*Kappel and Ryan*, 1986; *Karsten et al.*, 1986]. The bathymetry on the flanks is dominated by <300-m-high ridges that are parallel to the trend of the spreading center and are spaced uniformly ~6 km (0.2 Myr) apart. These ridges are interpreted as volcanic highs that formed periodically on the ridge axis and were then split apart by the inward facing normal faults that formed the axial valley [*Kappel and Ryan*, 1986]. The central Endeavour has been the focus of intensive study because it hosts five high-temperature vent fields [*Delaney et al.*, 1992; *Robigou et al.*, 1993; *Lilley et al.*, 1995; *Kelley et al.*, 2001] that are regularly spaced 2–3 km apart and are characterized by sulfide structures that are unusually large for intermediate spreading ridges.

[7] Many of the characteristics of the Endeavour segment suggest that it has a low magma supply. Regional monitoring [*Dziak and Fox*, 1995] and microearthquake experiments [*McClain et al.*, 1993; *Wilcock et al.*, 2002] show that the Endeavour supports high levels of seismicity. The presence of enriched mid-ocean ridge basalts on the ridge axis has been interpreted in terms of a low degree of melting as a result of a cooler mantle adiabat [*Karsten et al.*, 1990]. Side scan data [*Kappel and Ryan*, 1986; *Delaney et al.*, 1991] and seafloor observations [*Tivey and Delaney*, 1986] show that the axial valley is extensively faulted and fissured. These observations have been used to infer qualita-

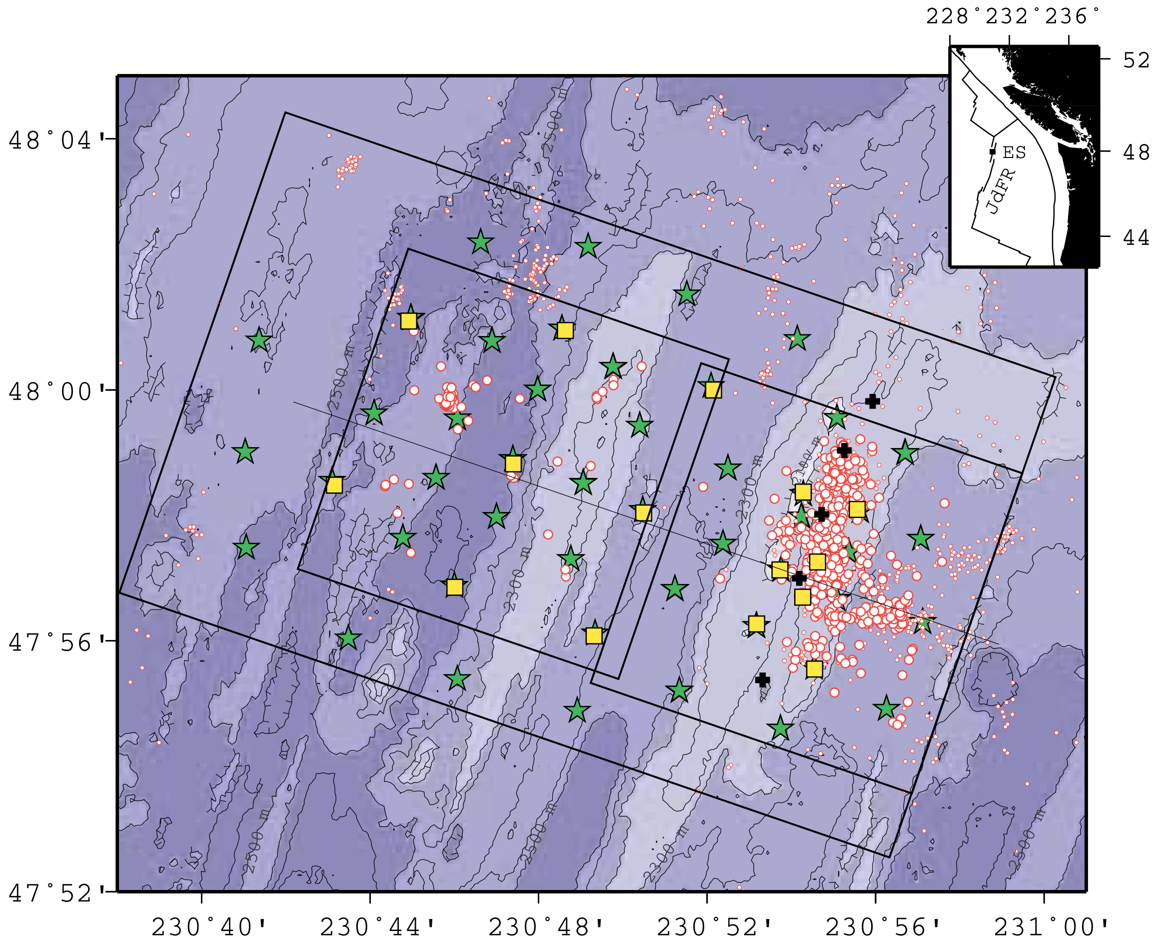

Figure 1. Bathymetric map of the Endeavour segment, contoured at 100 m intervals with color changes at 200 m, showing the location of receivers (filled yellow squares), explosive shots (filled green stars) and earthquakes (open red circles) for the 1995 microearthquake study [*Wilcock et al.*, 2002]. High temperature vent fields (black crosses) are also shown. The large box delimits the region of the active-source inversion and is the area covered by Figures 5 and 11 and the two smaller boxes show the regions of the on- and off-axis joint inversions. The earthquakes used in these inversions are shown by larger symbols. The faint line shows the orientation of the cross section shown in Figure 3.

tively that there have been no recent eruptions on this segment, but the youngest volcanics have not been dated. The regular spacing of vent fields within the axial valley and the large size of the sulfide structures suggest that hydrothermal circulation has had sufficient time to organize into a stable configuration without interference from eruptions [*Wilcock and Delaney*, 1996].

[8] Although the magma supply to the Endeavour may be affected by the ongoing reorganization of plate boundaries in the region because both ends of the segment are now dying rifts [e.g., *Karsten et al.*, 1990], the current configuration of the Endeavour has been attributed to normal cyclical processes on intermediate spreading ridges. *Kappel and Ryan* [1986] argue that the periodic topography on the flanks of the Endeavour and other segments of the Juan de Fuca Ridge is the result of cyclical variations in the relative importance of volcanism and tectonism. According to this interpretation, the Endeavour has just entered a tectonic stage as the central volcanic high has been rifted apart by the formation of the axial valley. One implication of this model is that the extrusive layer should be thicker beneath topographic highs.

[9] In 1995 we conducted a 55-day microearthquake experiment on the Endeavour (Figure 1) which recorded very high levels of seismicity both

on and off axis [*Wilcock et al.*, 2002]. Off-axis earthquakes on the Pacific plate are clearly affected by regional north-south compression associated with the deformation of the Explorer microplate. On axis, intense seismicity is concentrated at 2–3 km depth below the vent fields and the distribution of focal mechanisms is consistent with a stress field that is affected by hydrothermal cooling. This observation, coupled with the evidence for a low magma supply and the high heat flux from the vent fields, was cited as support for the hypothesis that the hydrothermal systems on the Endeavour are driven by a cracking front penetrating into the mid to lower crust [*Wilcock and Delaney*, 1996].

[10] A recent multichannel seismic (MCS) reflection experiment [*Carbotte et al.*, 2002; *Detrick et al.*, 2002; *Van Ark et al.*, 2003] shows that this hypothesis is wrong because the central Endeavour is underlain by a reflector at ~2.3–2.6 km depth [*Detrick et al.*, 2002] that has the negative impedance contrast expected of a magma lens [*Van Ark et al.*, 2003]. The reflector is at the same depth as a weak reflector imaged on a single MCS profile in 1985 [*Rohr et al.*, 1988]. Since the depth of the reflector is similar to the depth of axial earthquakes reported in the 1995 experiment [*Wilcock et al.*, 2002], joint interpretation of the MCS and earthquake data will require an understanding of the uncertainties in the inferred spatial relationships between the earthquakes and seismic reflector. One source of uncertainty is the bias in hypocenters and in particular focal depths that may result from errors in the velocity model used to locate the earthquakes.

3. Microearthquake Experiment Data Set

[11] The network for the 1995 microearthquake experiment [*Wilcock et al.*, 2002] comprised 15 Office of Naval Research ocean bottom seismometers (OBSs) deployed for 55 days along a 5 km section of the ridge axis near the Main vent field and up to 15 km off axis on the west flank (Figure 1). The OBSs recorded digital data at a 128-Hz sampling rate for four channels; three orthogonal 1-Hz seismometers and a hydrophone. Near the start of the deployment, 49 4.5-kg (10 lb) explosive charges were detonated within and around the network. The water wave travel times for these shots were used to locate the OBSs on the seafloor [*Wilcock et al.*, 2002]. The crustal *P* waves were also identified for each record and examples are shown in Figure 2a. The shot *P* waves have good signal to noise up to 20–30 Hz at all but the longest ranges and the picking uncertainty ranges from 8 to 32 ms with a root-mean square (RMS) value for all shots of 13 ms.

[12] A total of 1750 earthquakes were located with a minimum of one *S* wave and four *P* wave picks. Examples of records are shown in Figure 2b and in *Wilcock et al.* [2002]. The *P* wave arrivals for earthquakes within or near the network are generally impulsive with good signal to noise up to 20–50 Hz depending on the range and the picking uncertainties range from 10–60 ms with an RMS of 33 ms. The *S* wave arrivals tend to reverberate at frequencies near 10 Hz and the picking uncertainties vary from 20–150 ms with an RMS of 68 ms. Of the earthquakes, 1134 lie within 3 km of the nearest station and 670 are also within 1.5 km of the ridge axis. All of the earthquakes are located within the crust (Figure 3); the focal depths obtained using a one-dimensional model are clustered between 2 km and 4 km for off-axis earthquakes and between 2 km and just over 3 km for axial earthquakes. A narrow depth distribution is not ideal for joint inversions for hypocentral parameters and velocity and the earthquakes do not extend deep enough to constrain lower crustal structure. However, the earthquake data, coupled with *P* wave travel times for the explosive shots, provide an opportunity to constrain upper crustal structure and the trade-offs between velocity and hypocentral depths in the axial region.

4. Tomographic Method

[13] We used a seismic tomography method originally developed to invert controlled-source travel times for isotropic *P* wave velocity structure [*Toomey et al.*, 1994] and since extended to include seismic anisotropy [*Dunn and Toomey*, 1997; *Barclay et al.*, 1998], *S* wave velocities and hypo-

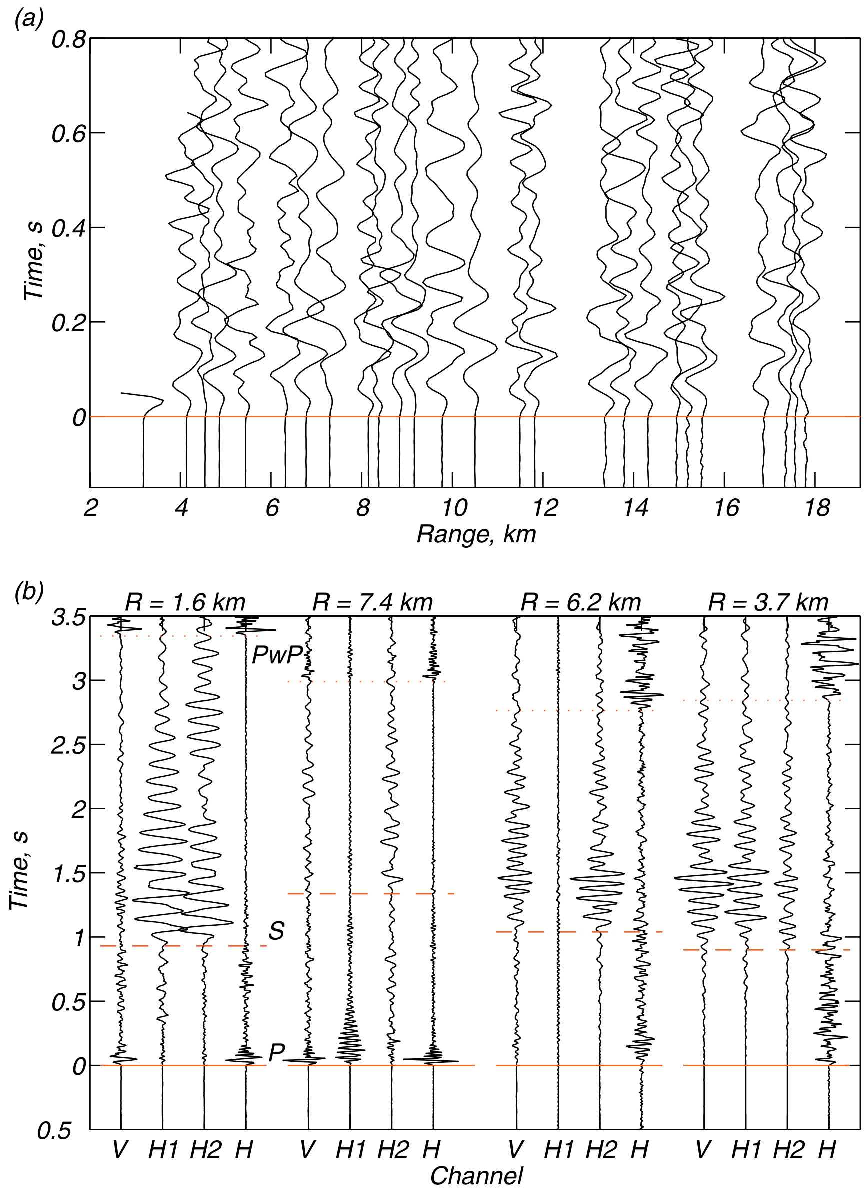

Figure 2. Examples of seismic records for explosive shots and earthquakes. (a) A subset of the explosive shot *P* wave arrivals recorded on the westernmost OBS plotted against range. The traces are aligned on the *P* wave pick (solid red line) and the water wave has been masked at shorter ranges. The traces have been scaled to equal maximum amplitude. (b) Four sets of earthquake records for the vertical channel (labeled V), two horizontal (H1 and H2) seismometer channels and the hydrophone channel (H). The traces are scaled to equal maximum amplitude except that the relative amplitude of the three orthogonal seismometer channels is preserved for each set of records. The left half of the plots shows records on two off-axis OBSs at ranges (*R*) of 1.6 km and 7.4 km for an earthquake near the northwesternmost OBS. The right half of the plot shows records on two axial OBS at ranges of 6.2 km and 3.7 km for an on axis earthquake located just to the north of the seismic network. The traces are aligned on the *P* arrival and arrival times are shown for *P* waves (solid red line), *S* waves (dashed red line), and for the *PwP* phase (dotted red line). The *PwP* phase is a *P* arrival with one reverberation in the water column at the end of its path. Note that for the second and third set of records, the first horizontal channel has bad data because the seismometer was poorly leveled.

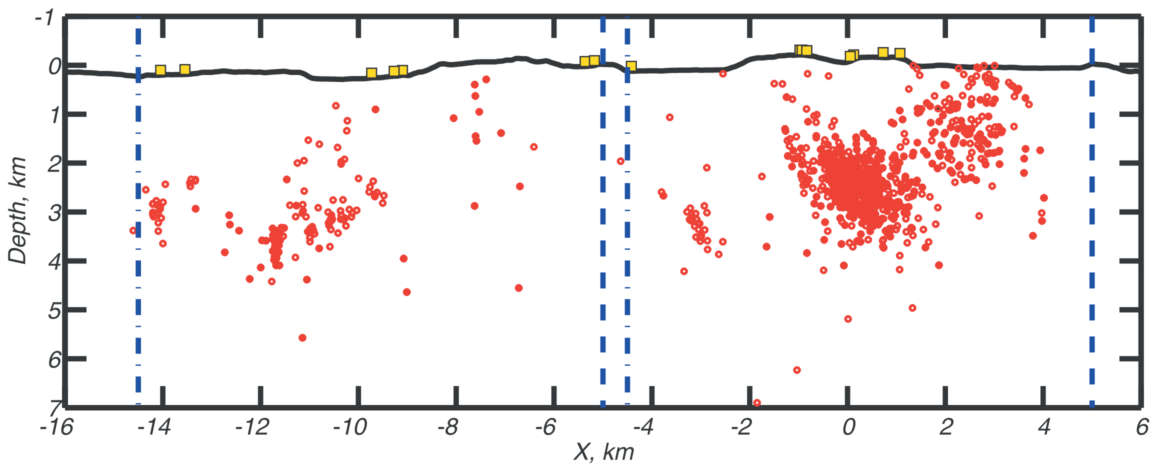

Figure 3. Cross section oriented perpendicular to the ridge showing the projected location of earthquakes with well resolved focal depths (red circles) and stations (filled yellow squares) [*Wilcock et al.*, 2002]. Vertical dashed and dot-dashed lines show the limits of the regions covered by the on- and off-axis joint inversions, respectively. The earthquakes used in these inversions are shown by filled symbols. The ridge axis is located at x = 0 km.

central relocation [*Barclay et al.*, 2001]. For the forward problem the P and S wave velocity models are defined on a three-dimensional grid of nodes that are spaced at 250 m. Travel times and ray paths are calculated using the shortest-time algorithm [*Moser*, 1991], modified to include the effects of seafloor relief by shearing the velocity grid vertically and by interpolating the seafloor ray-entry points at 100 m spacing on a two-dimensional grid. P and S wave travel times are calculated separately unless the V_P/V_S ratio is constrained to be constant everywhere. For P waves, the percent magnitude and direction of anisotropy may be specified at each node. Hexagonal anisotropy is assumed to have a cos(2θ) velocity variation, where θ is the angle between the ray direction and the fastest anisotropy direction. The percent anisotropy is defined as $(V_{max} - V_{min})/V_{average}$, where V_{max}, V_{min} and $V_{average}$ are the maximum, minimum, and direction-averaged wave speeds, respectively. On the basis of observations of P and S wave anisotropies on the Endeavour segment [*Almendros et al.*, 2000] and other mid-ocean ridges [*Shearer and Orcutt*, 1985; *Stephen*, 1985; *Sohn et al.*, 1997; *Barclay et al.*, 1998; *Dunn and Toomey*, 2001; *Barclay and Toomey*, 2003], we assumed that the anisotropy symmetry axis was everywhere horizontal and parallel to the plate-spreading direction. For hexagonal symmetry, the fastest P waves propagate in the plane that is perpendicular to the symmetry axis.

[14] The inverse method solves for perturbations to starting models of P and S wave slownesses and hypocenters (x, y, z, and origin time) using the LSQR algorithm [*Paige and Saunders*, 1982]. The perturbational models are defined on a three-dimensional grid that is distinct from the velocity grid and has 1 km and 0.5 km spacing in the horizontal and vertical directions, respectively. Several iterations of ray tracing and inversion are used until the perturbations become insignificant.

[15] The inverse problem can be expressed as the minimization of

$$s^2 = \mathbf{d}^{\mathbf{T}}\mathbf{C}_{\mathbf{d}}^{-1}\mathbf{d} + \sum_{i=1}^{15} \lambda_i \mathbf{m}^{\mathbf{T}}\mathbf{C}_i^{-1}\mathbf{m}, \qquad (1)$$

where $\mathbf{m}$ is a vector of perturbational model parameters, and $\mathbf{d}$ contains the travel and/or arrival time misfits. The data covariance matrix, $\mathbf{C_d}$ is a diagonal matrix containing estimates of the variance in each observation. The right hand term represents a series of constraints that regularize and control the inversion, where $\mathbf{C}_i$ and λ_i are the model covariance matrix and the weighting for the ith constraint and the vector $\mathbf{m}$ can be written as

$$\mathbf{m} = \begin{bmatrix} \mathbf{u}_P \\ \mathbf{u}_S \\ \mathbf{h} \\ \mathbf{s}_P \\ \mathbf{s}_S \end{bmatrix}, \qquad (2)$$

where $\mathbf{u}_P$ and $\mathbf{u}_S$ are the P and S wave slowness model vectors, $\mathbf{h}$ is a vector of the earthquake hypocentral parameters and $\mathbf{s}_P$ and $\mathbf{s}_S$ are vectors of the station corrections for P and S waves. Vectors $\mathbf{d}$ and $\mathbf{m}$ are related by a sparse partial derivative matrix $\mathbf{G}$, such that $\mathbf{Gm} = \mathbf{d}$. The constraints in equation (1) are summarized in Table 1. They implement damping and smoothing of the slowness parameters, damping of the V_P/V_S ratio and hypocentral parameters, and damping and averaging of station corrections.

[16] The method we used differs from that of *Barclay et al.* [2001] in two respects. For some of our inversions that involved one-dimensional velocity structure, we solved for P and S wave station corrections in order to account for the effects of near-receiver velocity variations. This modification required the addition of a penalty constraint for each station correction and the constraint that the mean station corrections for P and S waves are zero across the seismometer network. For P waves these constraints can be written

$$\lambda_{12} \sum_{j=1}^{N} S_{P,j}^2 = 0, \qquad \lambda_{14} \sum_{j=1}^{N} S_{P,j} = 0, \qquad (3)$$

where N is the number of stations and S_{Pj} is the station correction for the jth station.

[17] We also modified the penalty constraints on the hypocentral depth to force the mean perturbation to change by a chosen amount at specified iterations, allowing us to explore the trade-offs between hypocentral depth, origin time and velocity structure. The modified constraint can be written

$$\lambda_{10} \sum_{k=1}^{M} \left(h_{z,k} - z_b\right)^2 = 0, \qquad (4)$$

Table 1. Constraints for the Tomographic Inversions

Constraint Number, i	Description	Acts On	Reference	Constraint Weight, λ_i[a]: Shot 1-D	Shot 3-D	Joint 1-D	Joint 1-D, Depth-forcing
1	*P* wave slowness damping	u_P	*Toomey et al.* [1994]	100 (10–500)	2000 (100–1000)	1 (1–1000)	1
2	*S* wave slowness damping	u_S	*Toomey et al.* [1994]	–	–	10 (10–10000)	10
3	*P* wave slowness vertical smoothing	u_P	*Toomey et al.* [1994]	50 (10–100)	30 (10–500)	100 (1–500)	100
4	*P* wave slowness horizontal smoothing	u_P	*Toomey et al.* [1994]	10000	30 (10–500)	10000	10000
5	*S* wave slowness vertical smoothing	u_S	*Toomey et al.* [1994]	–	–	1	1
6	*S* wave slowness horizontal smoothing	u_S	*Toomey et al.* [1994]	–	–	10000	10000
7	V_P/V_S constraint	u_P, u_S	*Barclay et al.* [2001]	–	–	10 (10–10000)	10
8	Hypocenter x coordinate damping	h	*Barclay et al.* [2001]	–	–	0.01 (0.01–1)	0.01
9	Hypocenter y coordinate damping	h	*Barclay et al.* [2001]	–	–	0.01 (0.01–1)	0.01
10	Hypocenter z coordinate damping	h	*Barclay et al.* [2001], this paper	–	–	0.01 (0.01–1)	0.01
11	Hypocenter origin time damping	h	*Barclay et al.* [2001]	–	–	0.01 (0.01–1)	0.01
12	*P* wave station correction damping	s_P	this paper	–	–	1 (0.01–100)	0.01
13	*S* wave station correction damping	s_S	this paper	–	–	1 (0.01–100)	0.01
14	*P* wave station correction averaging	s_P	this paper	–	–	10000	10000
15	*S* wave station correction averaging	s_S	this paper	–	–	10000	10000

[a] Value used in inversion with the range of tested values given in parenthesis.

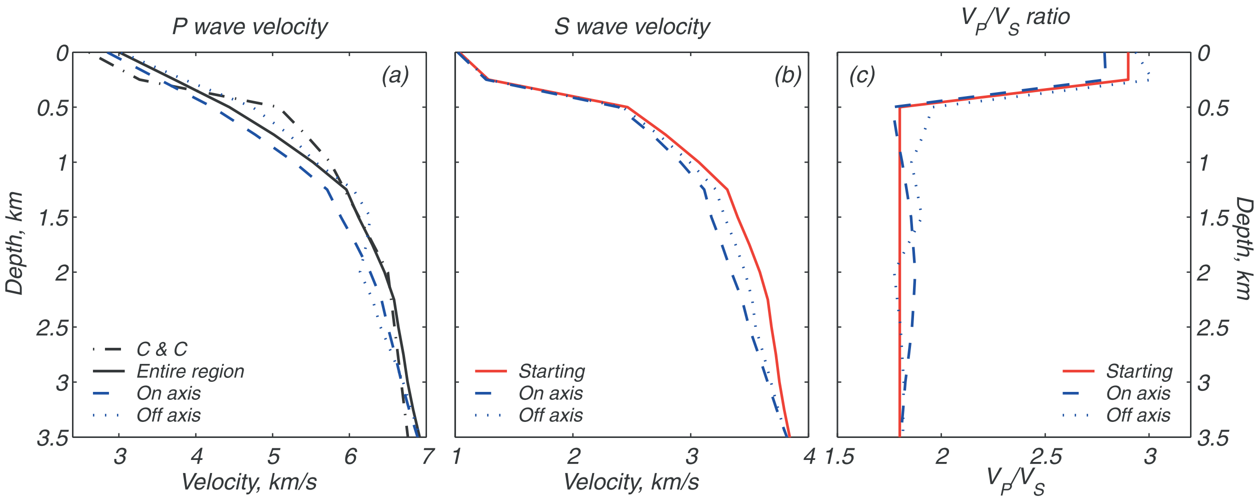

Figure 4. Results of inversion for one-dimensional, isotropic velocity structure showing (a) P wave velocity, (b) S wave velocity, and (c) V_P/V_S ratio. The *Cudrak and Clowes* [1993] P wave structure (labeled "C & C") was used as the starting model for the inversion of shot travel times, the result of which (labeled "Entire region") was used as the starting model for the on- and off-axis joint inversions. The starting S wave model for these inversions was derived assuming a V_P/V_S of 1.8 for nodes at depths $\geq$0.5 km and 2.9 for nodes at depths $\leq$0.25 km.

where M is the number of earthquakes, $h_{z,k}$ is the perturbation to the starting depth of the kth earthquake and z_b is a bias applied to change the mean depth of the hypocenters.

5. Inversions of Shot Data

[18] We applied the tomographic method in various ways to our data and conducted inversion of the explosive shots alone and joint inversion of the shot and earthquake data. The shots are uniformly distributed in and around the seismic network and these data were inverted for one- and three-dimensional isotropic structure and analyzed for anisotropy in a 19 km $\times$ 15 km area (Figure 1).

5.1. One-Dimensional Structure

[19] We first inverted the shot travel time data for the best fitting isotropic, one-dimensional P wave velocity model. We did this in order to obtain a starting model for the subsequent three-dimensional inversions and to test our data against an existing velocity profile from the Endeavour segment [*Cudrak and Clowes*, 1993]. The profile of *Cudrak and Clowes* [1993] was used as the starting model for the one-dimensional inversion and comprised the average of 10 seismic refraction lines that were centered on the Endeavour segment and extended out to ~15 km on both sides of the axis. In order to run the one-dimensional inversions, the horizontal smoothing weight λ_4 was set to a very large value. A variety of damping and vertical smoothing values were explored and the best model (Table 1) was chosen based on the goodness of fit and the smoothness of the profile.

[20] The starting and best-fit velocity profiles are shown in Figure 4a. The RMS misfits of the data to the starting and final best-fitting model were 80 ms and 66 ms, respectively, a variance reduction of 32%. The two models differ between the seafloor and 1.2 km depth. The structure derived by *Cudrak and Clowes* [1993] was based on the identification of layer 2A arrivals at short ranges on the refraction profiles and the matching of amplitudes as well as arrival times and as a result the velocities and velocity gradients in the shallow crust are well resolved. Our travel time inversions, by contrast, do not have good vertical resolution in the upper 1 km although the vertically averaged slownesses of the two models within this depth interval are similar. Below ~1.2 km depth both models were nearly identical and minor differences are likely

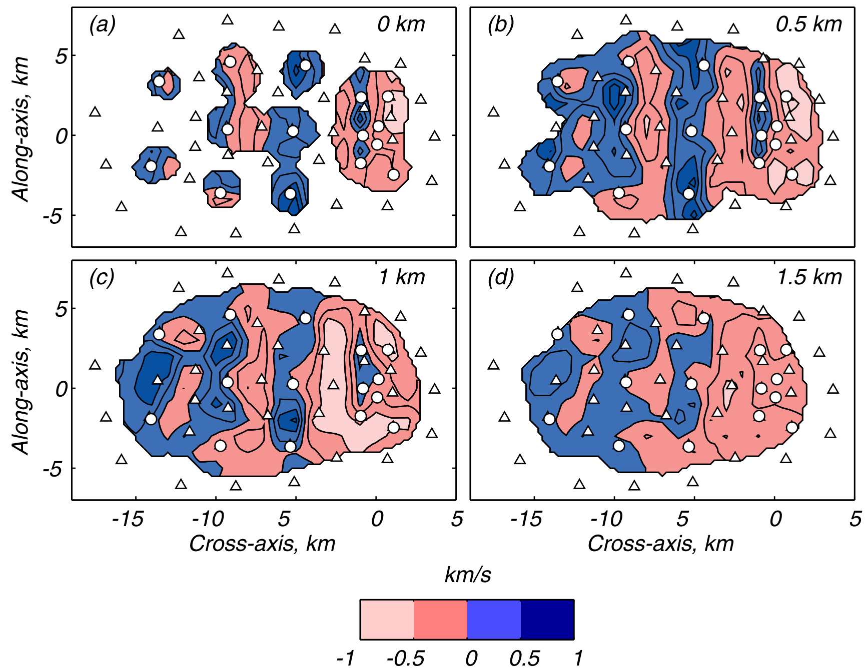

Figure 5. Results of inversion for three-dimensional isotropic *P* wave velocity structure. Contour plots of perturbations to the starting velocity structure (Figure 4a) on horizontal slices are shown at depths of 0, 0.5, 1 and 1.5 km. The contour interval is 0.25 km/s. Triangles represent shot positions and circles are receivers. The area of each slice is shown by the large box in Figure 1; regions of low sampling have been masked out.

due to differences in ray tracing, parameterization of the velocity structure, and the study area.

5.2. Three-Dimensional Structure

[21] The results of a tomographic inversion of the shot data for a three-dimensional isotropic model are shown in Figure 5. The image is the result of five iterations of the forward and inverse problems. The weighting of constraints in the inversion (Table 1) was based on fit to the data, the smoothness of the model, and the need to minimize spurious perturbations in regions of low ray coverage. The RMS travel time residual, 24 ms, represents an 87% variance reduction over the best fitting one-dimensional structure.

[22] The velocity model shows two systematic features. First, the seismic velocity variations averaged over the uppermost 1.5 km (Figure 6a) increase by about 8% from the axis to a crustal age of 0.5 Myr ($x = -15$ km). Second, eight axis-parallel, alternating bands of high and low velocity are superimposed on this increase. These bands are of width ~2 km and result in lateral velocity variations of ~1 km/s. Superimposed on these systematic features are additional lateral variations of up to ~0.25 km/s. In many places these are close to receiver locations in the shallowmost slices and they are likely due to near-surface velocity heterogeneity and/or uneven ray distribution.

[23] Figure 7 shows contour plots for the derivative weight sum (DWS), an estimate of ray density [*Toomey et al.*, 1994] for the inversion of Figure 5. At all depths, the DWS is highest beneath the ridge axis owing to the high density of near-axis seismometers. However, at depths of 1 and 1.5 km, the ray density is relatively high and smooth everywhere within the tomographic images, and we conclude that the lateral seismic velocity variations are well resolved. The density of rays is less smooth at shallow depths with significantly better sampling beneath the seismometers. As the positions of the seismometers also correspond to many of the small-amplitude velocity variations at 0 and 0.5 km in Figure 5, we attribute these variations to either velocity or sampling heterogeneity.

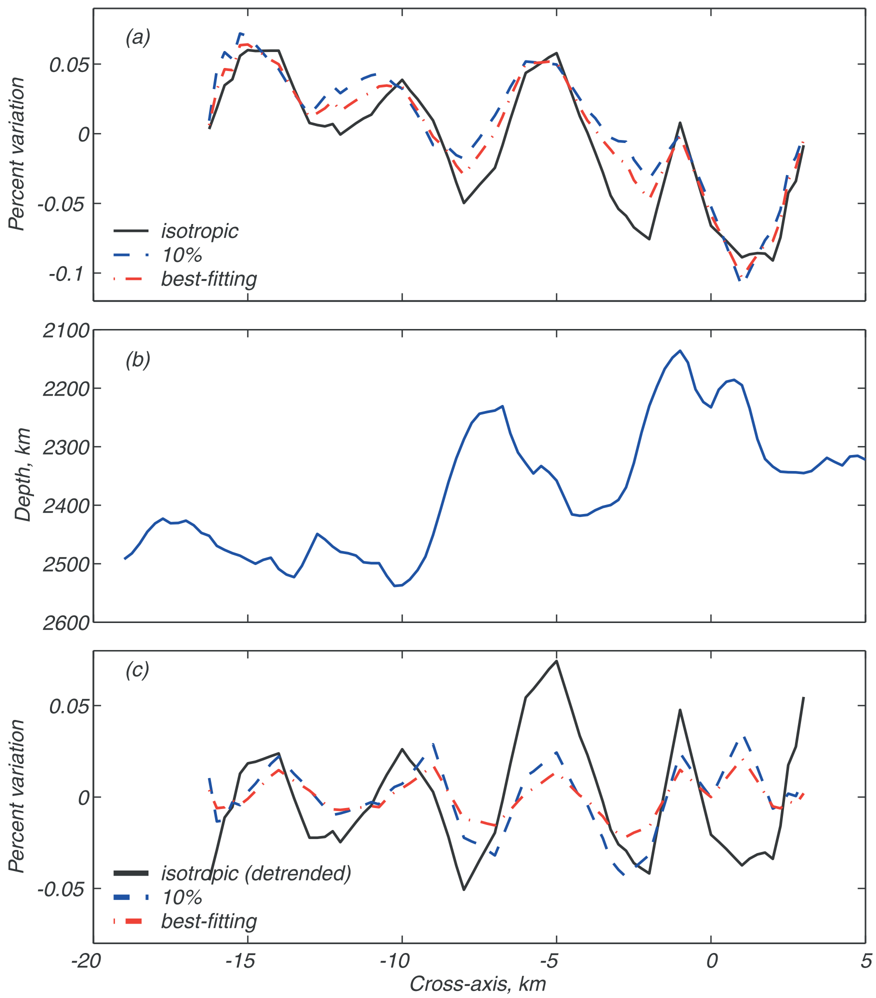

Figure 6. Cross-axis variation in P wave velocity and bathymetry. The ridge axis is located at $x = 0$ km. (a) Percent variation of three-dimensional P wave slowness structure (relative to the starting model), averaged in the along-axis direction and between 0 and 1.5 km depth. The mean depth-averaged velocity is 0.22 s/km. Results from inversions of data assuming isotropy (Figure 5), constant 10% anisotropy, and the best-fitting anisotropy structure (Figure 8f) are plotted against cross-axis distance. (b) Bathymetry averaged in the axis-parallel direction. (c) As for (a), but with results from three-dimensional, isotropic inversions of synthetic data sets that were generated for models with constant 10% anisotropy and the best-fitting structure. The detrended variation for the isotropic data inversion is also shown.

[24] The axis-parallel bands show an inverse correlation with the bathymetry. This is apparent from comparing the averaged percent velocity variation (Figure 6a) with the average bathymetry in the along axis direction (Figure 6b). Away from the ridge axis, the high-velocity bands are consistently located near bathymetric lows. The peak-to-peak amplitude of the velocity variation decreases westward, from 12% at $x = -5$ km to 5% at $x = -15$ km. Near the ridge axis, the correlation between velocities and bathymetry is less apparent and the western half of the axial volcanic high ($x = -2$ km) is underlain by high velocities.

5.3. Seismic Anisotropy

[25] The tomographic image in Figure 5 assumes an isotropic crust. However, seismic P and S wave anisotropy in the upper oceanic crust has been noted at several sites [*Shearer and Orcutt*, 1986; *Sohn et al.*, 1997; *Barclay et al.*, 1998; *Dunn and Toomey*, 2001] and is usually attributed to the preferential alignment of cracks normal to the plate

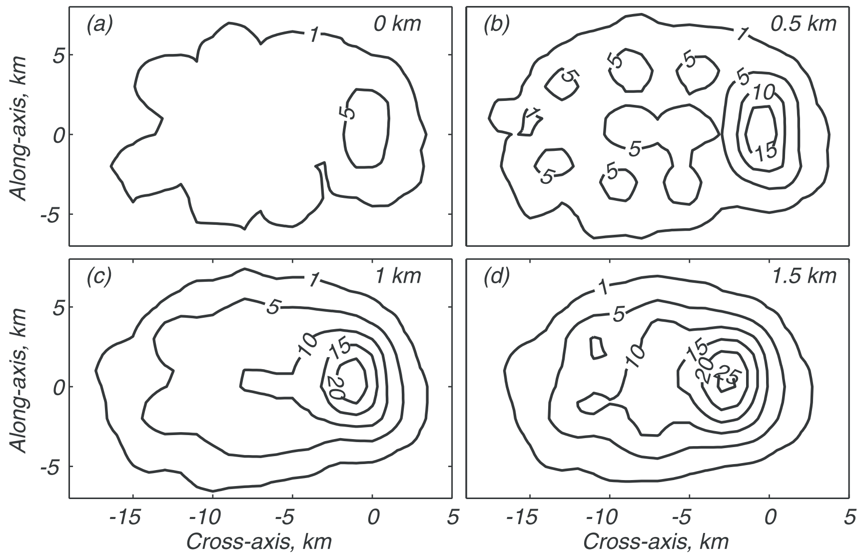

Figure 7. Derivative weight sum (DWS) for the set of ray paths used in Figures 5 and 11, contoured at values of 1, 5, 10, 15 and 20. The DWS is a weighted sum of the length of ray paths that influence a model parameter [*Toomey et al.*, 1994] and thus an estimate of ray density.

spreading direction. Crack anisotropy at the Endeavour segment has been inferred from the splitting of *S* wave arrivals from microearthquakes [*Almendros et al.*, 2000]. For *P* waves a hexagonal anisotropy system has the effect of modifying the isotropic *P* wave velocity with a cos(2θ) azimuthal variation, the slowest velocities being perpendicular to the crack alignment. Although a cos(4θ) variation is also predicted [*Crampin*, 1993], its effect on travel times is especially difficult to separate from isotropic heterogeneity and is rarely reported [e.g., *White and Whitmarsh*, 1984]. The relatively low ray density in our experiment is not ideal for separating anisotropy from heterogeneity and we therefore attempted to establish the existence of an anisotropic signal in the data and to assess its effect on the heterogeneous isotropic structure.

[26] Figures 8a–8e shows the travel time residuals for the best-fitting isotropic model (Figure 5), plotted as a function of source-receiver azimuth and grouped by turning depth. There is a clear cos(2θ) signal in the plots, with the minimum residual in the along-axis direction, consistent with an anisotropic signal. We measured the amplitude of the signal, and converted this to percent *P* wave anisotropy assuming that the source-receiver distance was the length of a ray traveling at the velocity of the turning depth. The resulting depth-dependent anisotropy structure (Figure 8f) shows anisotropy decreasing sharply from 9% at 0.75 km depth to ∼1% at depths greater than 2 km. The average value for all arrivals is ∼3%.

[27] We also estimated the level of anisotropy by repeating the three-dimensional inversions of the shot data with different percentages of fixed uniform anisotropy. The resulting RMS travel time misfit (Figure 9) shows a clear minimum between 4 and 5% that is close to the average value of 3% estimated from the residuals for the best-fitting isotropic model. A plot of the mean travel time residual versus source-receiver azimuth for a variety of imposed anisotropy models (Figure 10) shows that the depth-dependent model of Figure 8f flattens out the azimuthal variations in the residuals that are seen for the isotropic inversion. The residuals become increasingly overcorrected as the imposed anisotropy is increased to 10% (Figure 10).

[28] It is possible that the banding in the velocity structure in Figure 5 could be a result of anisotropy. Away from the ridge axis, all of the OBSs were deployed near bathymetric lows because these

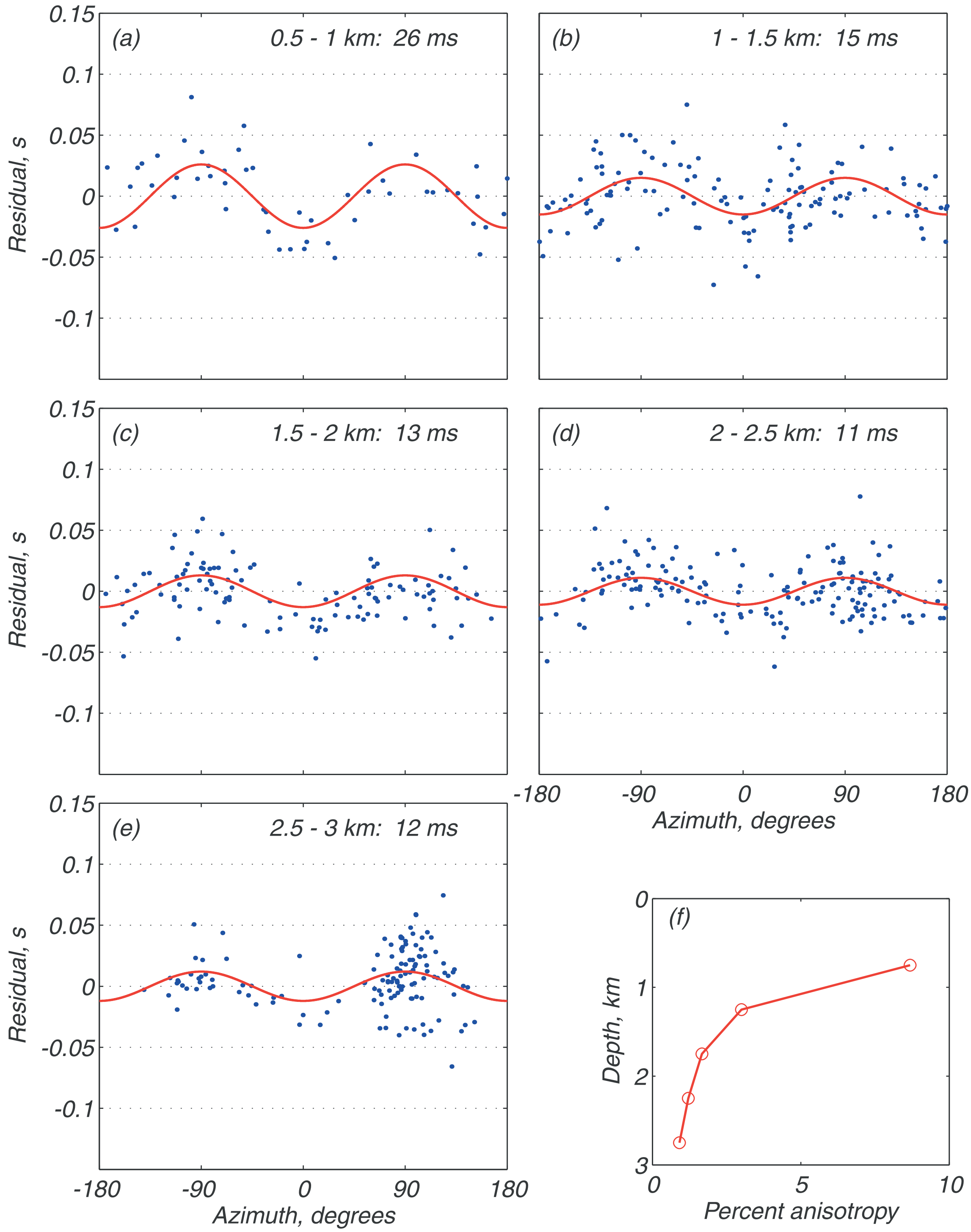

Figure 8. Travel time residuals from the isotropic, three-dimensional model versus source-receiver azimuth for different turning depths. (a–e) Residuals for rays turning at 500 m intervals from 0.5 km to 3 km depth. The best-fitting cos(2θ) curve, constrained to have minima in the direction parallel to the trend of the ridge axis, is superimposed on each plot; the amplitude of each curve is labeled in the upper right. (f) Depth-dependent anisotropy structure, derived from the best-fitting curves (Figures 8a–8e).

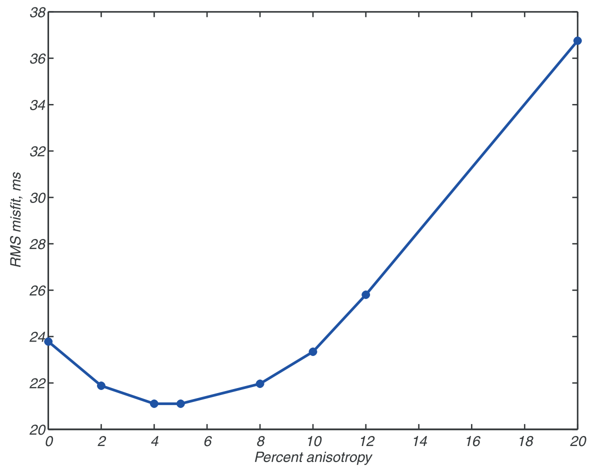

Figure 9. RMS travel time residual for three-dimensional inversions of the shot data versus assumed constant percent anisotropy.

regions have thin layers of sediment and the smoother terrain increases the probability that the freefall OBSs will deploy in a level orientation. If the OBSs are in lows then all the ray paths with fast ridge parallel orientations will also be aligned along bathymetric lows and this may bias the isotropic velocities beneath these regions to higher values.

[29] We took two approaches to assess the degree of mapping from anisotropy into heterogeneity. First, we calculated sets of travel times for the one-dimensional starting model combined with two separate anisotropy models: the best fitting anisotropy structure shown in Figure 8f and a conservatively high 10% constant anisotropy structure. We inverted these travel times assuming an isotropic structure with the same inversion parameters as used for the inversion of Figure 5. The resulting velocity model for 10% anisotropy is shown in Figure 11. It shows alternating high- and low-velocity axis-parallel bands resembling those in Figure 5 although they appear less pronounced because there are larger velocity variations in the ridge parallel direction. We compared the percent velocity variations averaged over the upper 1.5 km

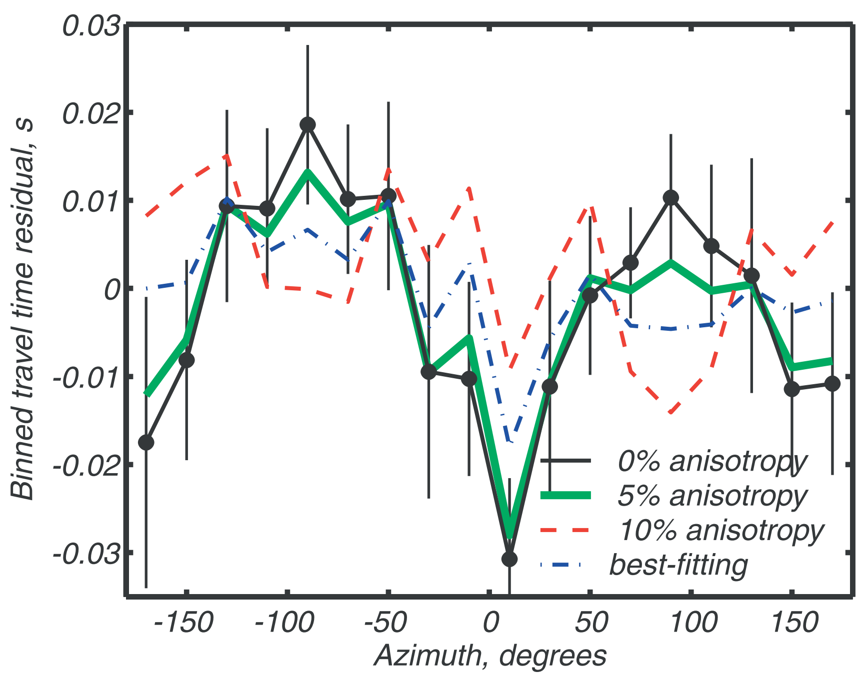

Figure 10. Mean travel time residual versus source-receiver azimuth for a variety of imposed anisotropy models. Means are determined at 20° azimuth intervals. The curves depict the residuals for imposed anisotropy of 0, 5, and 10% and the depth-dependent structure of Figure 8f. The source-receiver azimuth is measured at the receiver and clockwise with respect to the trend of the ridge axis, which strikes at N19°E. The vertical bars on the curve for zero anisotropy represent the 95% confidence ranges for each mean determined using the Student's t test and are also applicable to the corresponding residuals for the anisotropic models.

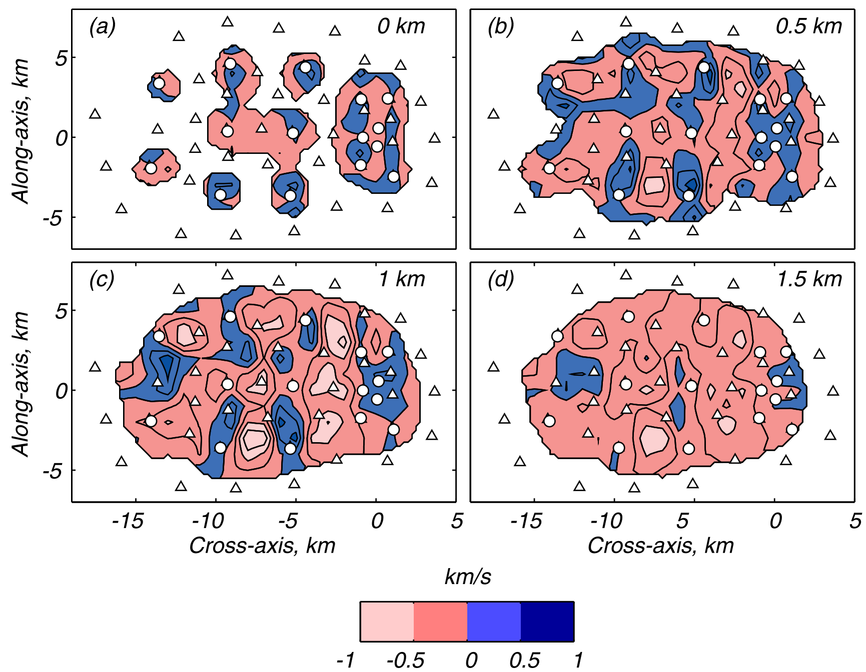

Figure 11. Results of synthetic test for anisotropy. Synthetic travel times were created for a velocity structure with 10% anisotropy assuming a one-dimensional model obtained by inverting the shot data (solid line in Figure 4a), and were then inverted for isotropic velocity structure. (a–d) Contour plots of *P* wave velocity perturbations to the starting velocity structure at depths of 0, 0.5, 1 and 1.5 km respectively. The plotting conventions are the same as for Figure 5.

in the along axis direction for these synthetic inversions with the detrended curve for isotropic inversion of the real data (Figure 6c). For the best fitting model, the percentage variations in the synthetic inversions are about one third those in the true inversions and even for 10% anisotropy, the percentage variations in the synthetic inversions are smaller than those obtained for the true inversion and this is particularly clear 3–8 km off axis. Thus we infer from this test that anisotropy may have contributed to the axis-parallel banding but is unlikely to account for the entire signal.

[30] Second, we looked at the isotropic signal in the three-dimensional inversion of the true data assuming the depth dependent anisotropy model of Figure 8f and a constant anisotropy of 10%. The RMS misfit for the imposed depth-dependent anisotropy model (19 ms) was lower than for the isotropic (RMS = 24 ms) and 10% imposed constant anisotropy (RMS = 22 ms) models. As expected, increased anisotropy modifies the averaged percent velocity variation and generally reduces the amplitude of the banding (Figure 6a). However, the effect is relatively small and even with 10% anisotropy the amplitude of the banding still exceeds half the value for the isotropic inversion. Again we conclude that anisotropy may be responsible for some of the heterogeneity but that the banding in the isotropic inversion of Figure 5 is not entirely due to anisotropy.

6. Inversions of Earthquake and Shot Data

[31] We jointly inverted arrival times from microearthquakes and the shots in order to determine the *S* wave velocity structure and better understand the trade-off between hypocentral depths and velocity structure near the axis. We considered data subsets within two 10 km by 10 km areas (Figure 1); one centered on the ridge axis and the other 9.5 km off-axis. Because of the relatively small number of earthquakes within the uppermost 2 km of the crust, we anticipated large trade-offs between

velocity structure and hypocentral parameters and we restricted our joint inversions to one-dimensional P and S wave velocity structures. The axial area includes a higher density of earthquakes and here we explored the trade-offs between focal depth and velocity by adding forcing constraints to the mean hypocentral depth.

6.1. One-Dimensional Inversions

[32] We inverted subsets of the data for one-dimensional P and S wave velocity structures within the on-axis and off-axis subregions (Figure 1). The starting P wave velocity structure was the best-fitting one-dimensional structure obtained from the shot data (Figure 4). The starting S wave velocity structure was derived from the P wave structure assuming a V_P/V_S ratio that was fixed to 2.9 at depths $\leq$0.25 km and to 1.8 at depths $\geq$0.5 km. An average V_P/V_S of 1.8 has been determined for the upper oceanic crust by several studies [*Shearer*, 1988; *Barclay et al.*, 2001] while an average value of 2.9 is consistent with the high Poisson's ratios inferred for layer 2A [*Collier and Singh*, 1998; *Barclay et al.*, 2001]. These values are also consistent with the analysis of the Endeavour microearthquake data [*Wilcock et al.*, 2002]. For the earthquakes we used starting hypocentral parameters determined with HYPOINVERSE [*Klein*, 1978] by *Wilcock et al.* [2002] and we used this data set to extract the earthquakes falling more than 500 m within the model limits and with at least two S wave and four P wave arrivals. A total of 465 earthquakes, 8 OBSs and 17 shots were used for the axial inversions; the corresponding values for the off-axis inversions were 79, 8, and 17 respectively. Independent P and S wave station corrections were included in the inversions and nine iterations of the forward and inverse problems were used in each inversion to obtain the best-fitting structure. From a range of inversions using different constraints (Table 1) we chose the best fitting set of model parameters that were also physically realistic.

[33] The best fitting models for the one-dimensional inversions are shown in Figure 4. The RMS residuals for the earthquake P and S wave arrival times and the shot travel times respectively are 60, 34, and 67 ms for the axial region and 55, 65, and 35 ms for the off-axis inversion. The P wave velocities for the on-axis inversion are <0.3 km/s lower than for the starting model at all depths down to $\sim$2 km. For the off-axis region, the velocities are <0.2 km/s higher at depths shallower than 1.5 km and $\sim$0.1 km/s lower at greater depth. Below 2.5 km the magnitude of perturbations to the starting model is <0.1 km/s for both inversions. The differences between the on- and off-axis structures are in agreement with the active-source results for the entire region (Figures 4 and 5) that show an increase in seismic velocity as the crust ages.

[34] The best-fitting S wave velocity structures (Figure 4b) are both lower than the starting model at all depths, with the on-axis velocities lower by up to 0.2 km/s and everywhere lower than the off-axis result for which the maximum reduction is $\sim$0.1 km/s. Beneath 0.5 km, the V_P/V_S results (Figure 4c) are on average slightly greater than the assumed starting value of 1.8. Above 1 km, V_P/V_S is markedly higher off axis than on axis.

[35] Because the density of earthquakes is highest on the ridge axis, we attempted three-dimensional inversions of shots and earthquake travel times in this region. However, inspection of the resulting models and the results of checkerboard resolution tests show that with the exception of shallow regions imaged by the shots, the distribution of data is insufficient to resolve even long-wavelength three-dimensional structure.

6.2. Trade-Off Between Velocity and Focal Depth

[36] Most of the earthquakes on the ridge axis were located in the depth range 2–3 km with few events at depths shallower than 1.5 km [*Wilcock et al.*, 2002]. With no P wave velocity constraints from the shot travel times below 1.5–2 km depth and no independent constraints at all on the S wave velocity structure, hypocentral parameters (especially depth and origin time) may trade off against seismic velocities and station corrections. To better understand the trade-offs between focal depth and velocity structure in the axial region, we increased

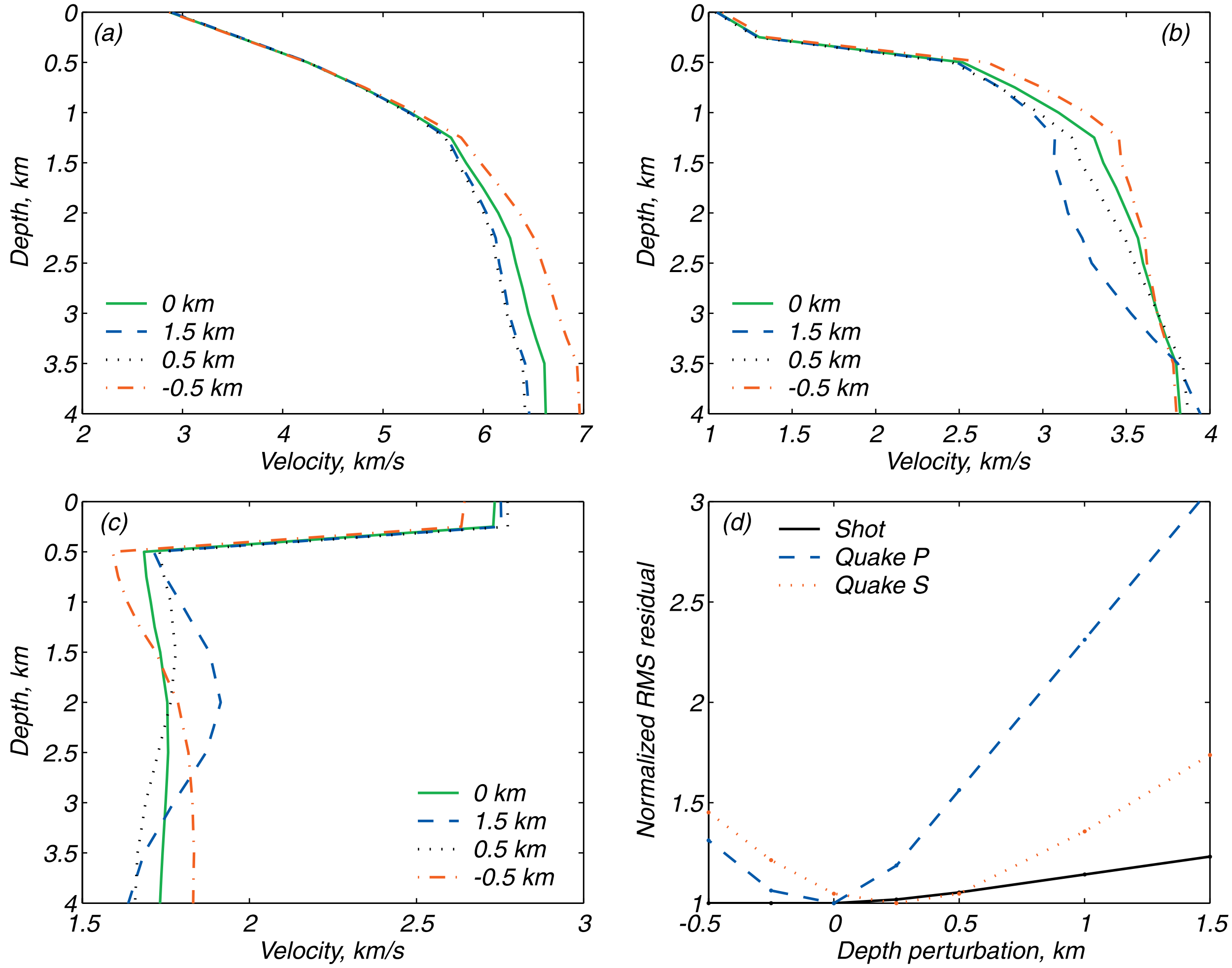

Figure 12. Results of joint inversions for one-dimensional velocity structures and hypocenters with the average hypocentral depths progressively forced. (a) *P* wave velocity profiles. (b) *S* wave velocity profiles. (c) V_P/V_S profiles. (d) RMS of the misfit, for the shot, earthquake and all arrivals versus forced depth perturbation. In each case the RMS is normalized with respect to the minimum. Depths were forced in 0.25 km steps to 1.5 km deeper (positive perturbation) and 0.5 km shallower (negative depth perturbation) than the best fitting solution.

and decreased the earthquake starting depths and inverted for the model parameters that best fit the data under the constraint of zero average depth perturbation. The average depth was perturbed in 0.25 km increments from 0 km to 1.5 km deeper and from 0 to 0.5 km shallower. Solutions with a larger perturbation to shallower depths are not presented because they led to a significant number of earthquake hypocenters above the seafloor. For each perturbation, five inversions of the forward and inverse problems were used to find the best-fitting model. The damping and smoothing constraints on all parameters were kept low in order to maximize the fit (Table 1). For all of the inversions the hypocenters, after correction for the imposed depth perturbation, typically moved no more than 100 m from the locations shown in Figure 3.

[37] The results are summarized in Figure 12. The RMS residuals for the earthquake *P* and *S* waves are minima for focal depth perturbations of 0 km and 0.25 km respectively (Figure 12d) and increase by 10–20% for depth perturbations of ±0.5 km. As the earthquakes are forced deeper, there is a tendency for both *P* and *S* wave velocities to decrease. For *P* waves (Figure 12a), the strong constraints from the shot data inhibit changes above ~1.5 km depth and the velocities are essentially unchanged

in the upper 1 km. For an 0.5 km increase in average focal depths, the P wave velocity decreases below 1.5 km depth by up to ~0.2 km/s. The S wave velocity also decreases at all depths (Figure 12b) and V_P/V_S increases slightly above 2 km depth and decreases at greater depths (Figure 12c). The P wave station corrections are insensitive to the focal depth but the S wave station corrections become increasingly negative as the focal depth is increased. It may seem counterintuitive that velocities tend to decrease when the earthquakes are forced deeper but it can be shown that this effect is an expected result of the trade-off between velocities and origin time (Appendix A).

[38] The effects of forcing earthquakes 0.5 km shallower are essentially the opposite of forcing them 0.5 km deeper although the magnitude of the change in P and S wave velocities is slightly larger. The V_P/V_S ratio shows a pronounced minimum of 1.6 at 0.5-1 km depth and increases downward to values exceeding 1.8 below 2 km depth.

7. Discussion

[39] In this paper, we have presented a series of inversions of explosive shot and earthquake data from the Endeavour segment of the Juan de Fuca Ridge. The experiment geometry and depth of earthquakes is inadequate to image the mid- to lower-crustal low velocity zone that presumably underlies the ridge axis but the inversions do place strong constraints on upper crustal structure and the trade-off between velocity structure and the focal depths of axial earthquakes.

7.1. Increasing Shallow Velocities Off Axis

[40] The three-dimensional inversion of the shot data shows that the P wave velocities averaged over the upper 1.5 km increase by ~8% between crustal ages of 0 and 0.5 Ma. Comparisons of one-dimensional inversions of the shot and earthquake data for regions centered on-axis and 0.3 Myr off-axis show that the P wave velocity increases off-axis at all depths down to 2 km. The average change in the upper 1 km is nearly 10%. Interestingly, *Cudrak and Clowes* [1993] report no increase in velocities off axis from refraction experiment in the same area. This may be because they analyzed their data for lateral variations in both the velocity and thickness of layers 2A, 2B and 2C, an approach that may have obscured trends in the average velocity of layer 2. The average trends in velocity may also have been masked by heterogeneity along a limited number of refraction lines. Our inversions have lower resolution but average structure over a broader region.

[41] Our inversions have poor vertical resolution in the upper 1 km. An increase in upper crustal velocities with age is observed globally and is generally attributed to the sealing of porosity in layer 2A by hydrothermal processes [*Jacobson*, 1992]. An early synthesis of seismic data [*Houtz and Ewing*, 1976] suggested that velocities in layer 2A increased uniformly from 3.3 km/s near the ridge axis to 5.2 km/s at 40 Myr. However, more recent compilations show that velocities increase much more quickly in young crust [*Grevemeyer and Weigel*, 1996; *Carlson*, 1998]. If we attribute all the change in velocity we observe to a 400-m-thick layer 2A and assume a velocity of 2.6 km/s on-axis [*Cudrak and Clowes*, 1993], our data would require the velocity to increase by about 30% to 3.3 km/s by 0.5 Myr. This result is reasonably consistent with data from the East Pacific Rise which shows that layer 2A velocities increase by 45–50% between the spreading axis and 0.5–1 Myr [*Grevemeyer and Weigel*, 1997].

[42] *Rohr* [1994] used multichannel seismic reflection data to infer interval velocities for layer 2A on the heavily sedimented east flank of the Endeavour. The results show relatively constant velocities of 3.0–3.5 km/s up to 0.6 Myr followed by a steady increase in velocity to over 5 km/s by 1.2 Myr. *Rohr* [1994] correlates this change with increased basement temperatures as the hydrothermal regime changes from fully open to mostly closed under the thickening sediments. This explanation cannot account for our observations because we observe an increase at younger ages and the west flank is not heavily sedimented. While we cannot discount the possibility that evolution of layer 2A velocities up to 0.6 Myr is different on the two flanks, it seems more likely that the discrepancy reflects differences in the resolution of the two techniques.

The on-axis velocity (~3.3 km/s) and average thickness (650 m) inferred by *Rohr* [1994] for layer 2A are markedly different from the values of 400 m and 2.6 km/s obtained from refraction profiles in the same area [*Cudrak and Clowes*, 1993].

[43] The joint inversions of the shot and microearthquake data also show that S wave velocities increase off-axis at all depths down to 2 km. Below 1 km, the inversions predict $V_P/V_S = 1.8 - 1.9$ (equivalent to a Poisson's ratio $\sigma = 0.28 - 0.31$), values that are a little higher than most other studies [e.g., *Shaw*, 1994] but probably reasonable given the trade-offs between velocity and hypocentral depth. At shallower depths the S wave velocity increases less slowly with age than the P wave velocity. Between 0.5 km and 1 km V_P/V_S increases from 1.8 ($\sigma = 0.28$) on axis to values as high as 1.95 ($\sigma = 0.32$) off axis. This change may be an artifact of the limited resolution of our inversions but it could also be a result of the preferential sealing of thin cracks by hydrothermal processes [*Shaw*, 1994].

7.2. Banding of Shallow Velocity Structure

[44] The three-dimensional isotropic inversions of the shot data show ridge parallel bands of alternating high and low velocities that are best developed in the upper 1 km. Away from the ridge axis the shallow velocity is clearly correlated with topography. Our analysis shows that anisotropy may contribute to this signal but is unlikely to account for more than one third of the heterogeneity. Because our models have poor vertical resolution we cannot distinguish between a periodic change in the velocities of layer 2A and/or 2B or a change in the thickness of layer 2A. However, the observation that the amplitude of the banding decreases with age is consistent with the latter explanation given our inference that layer 2A velocities increase off-axis.

[45] Although the banding correlates strongly with the seafloor depth, we used a tomographic method that corrects for biases caused by bathymetry variations. The maximum travel time delay due to uncorrected bathymetry is ~50 ms (for a vertical ray traveling through 200 m of crust at 2.5 km/s compared to 200 m of water), and this is comparable to the ~30 ms delay that is responsible for the amplitude of the banding in Figure 6. The effect of bathymetry is accounted for, however, by shearing the velocity and perturbational grids to make them conformal with the seafloor. We also ruled out unevenly distributed or incorrectly calculated seafloor ray-entry points as possible sources of bias: the relief was low enough that the calculated rays entered the seafloor in troughs as well as on highs and the ray-entry point solutions were unique and robust.

[46] If we attribute all of the periodic signal to changes in layer 2A thickness our data require that layer 2A be 100–200 m thicker beneath bathymetric highs. This result is consistent with the interpretations of *Kappel and Ryan* [1986] who attributed the ridges to periods of increased volcanic activity. However, it is important to note that a 200 m change in extrusive layer thickness is a small perturbation to a system that generates 6 km of crust; the periodic ridges may not be indicative of large fluctuations in total magma supply.

[47] Near the ridge axis the correlation between bathymetry and shallow velocity is less clear since the bathymetric high to the west of the axial valley is underlain by high velocities. Here our results are difficult to interpret in terms of the model of *Kappel and Ryan* [1986]. A thinner layer of extrusives on the west side of the ridge axis might result from the displacement of the axial magma chamber to the east of the ridge axis [*Detrick et al.*, 2002].

[48] The lateral velocity heterogeneity in the shallowmost 1 km at the Endeavour segment can be compared with the results of similar tomographic experiments at the slow-spreading Mid-Atlantic Ridge (MAR) [*Barclay et al.*, 1998; *Magde et al.*, 2000] and at the fast spreading East Pacific Rise (EPR) [*Toomey et al.*, 1994]. At all three sites, the shots and receivers were distributed over a similar area (~300 km^2), were located away from ridge-axis offsets, recorded a large number of sea-surface sources on a smaller number of ocean-bottom seismometers, and used the same tomographic method.

[49] The comparison between the three sites is limited by the vertical and horizontal resolution

of the Endeavour experiment, which had the lowest density of sources of the three experiments. For example, we cannot state whether an EPR-like high velocity band is present directly beneath the Endeavour axial valley. We have interpreted the banding at Endeavour as variations in the thickness of layer 2A which is ~400 m thick [*Cudrak and Clowes*, 1993] but which is smeared to 1 km depth in the tomographic model. Even with these constraints, however, comparison can be made of the major features at the three sites.

[50] The Endeavour structure shares different characteristics of the EPR and MAR structures. The main features at the EPR and Endeavour (the high sub-axis velocities and the banding, respectively) are essentially invariant in the along-axis direction and reflect crustal accretion and deformation processes that are mainly two-dimensional. At the same time, the correlation between bathymetric highs and lower velocities is strong at both the Endeavour and MAR, suggesting that the processes responsible for the creation of the bathymetric highs in each case result in a thicker extrusive layer. The periodicity implied by the Endeavour structure may be considered to lie between the steady state EPR plate-spreading model [*Hooft et al.*, 1996] and the MAR where the structure is likely the result of a complex accretion history.

[51] Although there are significant differences between the velocity structures at the three sites, they are not necessarily representative of spreading rate. The slowly-varying morphology along fast spreading ridges suggests that the 9°N EPR site may be representative, but the split volcanic ridges that characterize the Endeavour site are not a constant feature of other intermediate-spreading segments which have a range of morphologies resembling both fast- and slow-spreading centers. At slow-spreading ridges, the large variations in along-axis morphology imply that a large number of tomography experiments would be necessary to establish a representative structure.

7.3. Anisotropy

[52] The shot data set is not adequate to support an inversion for anisotropy that discriminates between anisotropy and heterogeneity. Nevertheless it is clear from an analysis of the residuals of isotropic inversions that our data set includes an anisotropic signal. A cos(2θ) fit to the residuals at different turning depths suggests that the anisotropy is concentrated in the uppermost crust. The anisotropy of 9% inferred at 500–1000 m depth is rather high. The average value determined by this method for all the data is ~3% and agrees reasonably well with the value of 4–5% inferred from minimizing the residual of isotropic inversions. It is also reasonably consistent with studies at other ridges [*Sohn et al.*, 1997; *Barclay et al.*, 1998; *Dunn and Toomey*, 2001]. This apparent invariance of anisotropy with spreading rate is an interesting result since one could speculate the increasing importance of tectonic extension relative to volcanic extension at slower spreading rates might lead to increased fracture related anisotropy.

7.4. Depth of Axial Earthquakes

[53] The geometry of our experiment and the distribution of earthquakes near the ridge axis cannot resolve three-dimensional structure beneath the ridge axis. However, the joint inversions of axial data do provide a means to assess the trade-offs between one-dimensional velocity structure and focal depths (Figure 12). It is not possible to formally reject models on the basis of RMS. Since the changes is travel time RMS are fairly small for depth perturbations up to about ±0.5 km, all such solutions might be considered an adequate fit to the data.

[54] However, the velocity models obtained for a small increase in focal depth are probably more geologically plausible than those obtained for a small decrease. It is more likely that the seismic velocities in the axial region are anomalously low than anomalously high. The tomographic experiment of *White and Clowes* [1990, 1994] imaged a low velocity zone at 0.5–2 km depth with velocity anomalies of up to 0.3 km/s, a result that is not too inconsistent with the inversion with average focal depth perturbation 0.5 km deeper. In addition, the inversion with the average focal depth perturbed 0.5 km shallower leads to a V_P/V_S that decreases to 1.6 at 0.5 km depth. This is equivalent to a

Poisson's ratio, σ = 0.18 which lies well below the range of values reported for the oceanic crust [e.g., *Shaw*, 1994]. We infer that it is unlikely that the axial earthquakes are substantially shallower than reported by *Wilcock et al.* [2002] and that interpretations of axial processes on the Endeavour must account for the presence of microearthquakes near the axial magma chamber.

8. Conclusions

[55] 1. Average *P* wave velocities in the upper 1.5 km increase by ∼8% between crustal ages of 0 and 0.5 Ma. This increase is most likely due to the sealing of layer 2A porosity by hydrothermal processes. V_P/V_S between 0.5 and 1 km depth increases from 1.8 on axis to 1.95 off axis, possibly as a result of the preferred sealing of thin cracks below layer 2A.

[56] 2. The shallow *P* wave velocity structure is also characterized by axis-parallel alternating bands of high and low velocity with a peak-to-peak velocity variation of 5–12%. There is an inverse correlation away from the axial region between velocity variation and bathymetry, with low velocities associated with axis-parallel seafloor ridges. The velocity variations can be explained by a 100–200-m increase in layer 2A thickness beneath the split volcanic ridges.

[57] 3. There is a significant cos(2θ) azimuthal velocity variation in the *P* wave travel time residuals with respect to the best-fitting isotropic model. The residuals are best fit by a model with 9% anisotropy at 750 m depth decreasing to <1% at 3 km depth. The RMS travel time residual for inversions with constant anisotropy has a minimum at 4–5% anisotropy. The anisotropy is likely due to vertical cracks and fissures that are preferentially aligned in the along-axis direction. Although anisotropy may also contribute to the axis-parallel banding in the isotropic tomographic image, its effect is relatively small, with the best-fitting anisotropy model being responsible for about one third of the banding amplitude.

[58] 4. Trade-offs exist between the hypocentral depths of microearthquakes and the *P* and *S* wave velocity structures. Changing the mean hypocentral depth by up to 0.5 km leads to only modest increases in the travel time RMS but the resulting velocity models appear more feasible when the earthquakes are forced deeper. The axial earthquakes are unlikely to be substantially shallower than reported by *Wilcock et al.* [2002].

Appendix A: Trade-Offs Between Focal Depth and Velocities in Joint Inversions

[59] The effect of changing earthquake depths on the velocities obtained through joint inversions for velocity and hypocentral parameters can be understood by considering the simple two-dimensional configuration shown in Figure A1. Three stations are evenly spaced on a horizontal surface that overlies a medium of uniform seismic velocities. An earthquake occurs at time T_0 and depth Z beneath the central station and *P* wave arrival times are recorded at all stations and an *S* wave arrival time is recorded at the central station. The *P* wave arrival times on the exterior stations are identical and constrain the earthquake to lie beneath the central station. The travel times can be written in terms of *P* and *S* wave slownesses , U_P and U_S as

$$T_{P1} - T_0 = ZU_P, \tag{A1}$$

$$T_{S1} - T_0 = ZU_S, \tag{A2}$$

and

$$T_{P2} - T_0 = \frac{Z}{\cos\theta} U_P, \tag{A3}$$

where θ is the incidence angle for a ray traveling to an exterior station. If the depth of the hypocenter is now forced to change by ΔZ and the origin time and slownesses are allowed to adjust, the travel time equations become

$$T_{P1} - T_0 - \Delta T_0 = (Z + \Delta Z)(U_P + \Delta U_P), \tag{A4}$$

$$T_{S1} - T_0 - \Delta T_0 = (Z + \Delta Z)(U_S + \Delta U_S), \tag{A5}$$

and

$$T_{P2} - T_0 - \Delta T_0 = \left(\frac{Z}{\cos\theta} + \Delta Z \cos\theta\right)(U_P + \Delta U_P), \tag{A6}$$

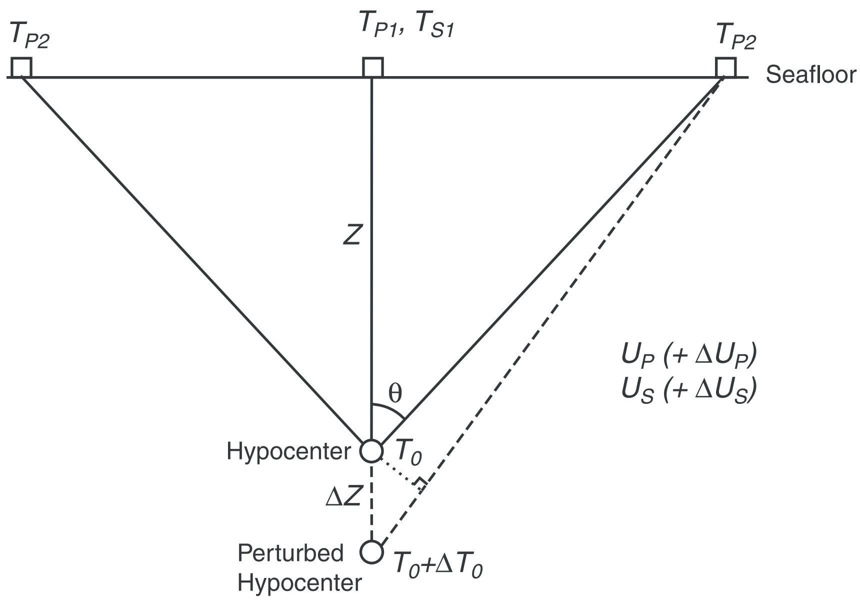

Figure A1. Cartoon showing the geometry of the initial (solid) and perturbed (dashed) ray paths used to calculate the effect on seismic velocities of changing the focal depth. The initial and perturbed earthquake hypocenters are shown by circles and the seismic stations by squares. The mathematical notation is defined in the text.

where ΔT_0 is the change in origin time, and ΔU_P and ΔU_S are the changes in P and S wave slowness respectively and we assume $\Delta Z \ll Z$ in equation (A6). Using equations (A1)–(A3) to substitute for T_{P1}, T_{P2}, T_{S1} and T_0 in equations (A4)–(A6) and solving for ΔT_0, ΔU_P and ΔU_S gives

$$\Delta T_0 = \frac{-Z\ \Delta Z\ U_P(1+\cos\theta)}{Z-\Delta Z\cos\theta} \approx -\Delta Z\ U_P(1+\cos\theta), \quad \text{(A7)}$$

$$\Delta U_P = \frac{\Delta Z\ U_P\ \cos\theta}{Z-\Delta Z\cos\theta} \approx \frac{\Delta Z}{Z} U_P\cos\theta, \quad \text{(A8)}$$

and

$$\Delta U_S = \Delta Z U_P \frac{((1-\phi)Z+(Z+\phi\Delta Z)\cos\theta)}{(Z+\Delta Z)(Z-\Delta Z\cos\theta)} \approx \frac{\Delta Z}{Z} U_P(1-\phi+\cos\theta), \quad \text{(A9)}$$

where

$$\phi = \frac{U_S}{U_P} = \frac{V_P}{V_S}, \quad \text{(A10)}$$

and the right hand expressions assume $\Delta Z \ll Z$.

[60] We can see that ΔU_P is positive when ΔZ is positive and hence the P wave velocity decreases when the earthquake is moved deeper. The corresponding change in origin time has two components. It moves earlier by a time $\Delta Z U_P$ to account for the increase in focal depth and by an additional time $\Delta Z U_P \cos\theta$ to account for the change in P wave velocity. For this geometry, the sign of ΔU_S is dependent on the aperture of the network. For a typical value of V_P/V_S = 1.8, the S wave velocity will decrease when the focal depth increases if $\theta < \mathrm{acos}(0.8) = 37°$.The change in V_P/V_S is given by

$$\Delta\phi = \frac{\Delta U_S U_P - \Delta U_P U_S}{U_P(U_P+\Delta U_P)} = -\frac{\Delta Z}{(Z+\Delta Z)}(1+\cos\theta)(\phi-1) \approx -\frac{\Delta Z}{Z}(1+\cos\theta)(\phi-1), \quad \text{(A11)}$$

and is always negative for an increase in focal depth.

[61] We can see from the inversions shown in Figure 12, that the changes in the P wave velocity are consistent with predictions of equation (A8) except at depths less than ~1 km where V_P velocities remain unchanged because they are strongly constrained by the explosive shot data. The S wave velocity and V_P/V_S models of Figure 12 are not consistent with equations (A9) and (A11). However, this is because the inversions of Figure 12 result in S wave station corrections that become increasingly negative as the average focal

depths are increased. If the station corrections are held fixed in the inversions, the changes in S wave velocity are more muted than shown in Figure 12b and V_P/V_S decreases at all depths.

Acknowledgments

[62] We thank Mike Purdy, the Woods Hole Oceanographic Institution OBS group and the captain and crew of the R/V *Wecoma* for their help in collecting the data. Constructive reviews were provided by Robert Dunn, Robert Sohn, and Jim Gaherty, the Associate Editor. This work was supported by the National Science Foundation under grants OCE-9403668 and OCE-9907170.

References

Almendros, J., A. H. Barclay, W. S. D. Wilcock, and G. M. Purdy (2000), Seismic anisotropy of the shallow crust at the Juan de Fuca Ridge, *Geophys Res. Lett.*, *27*, 3109–3112.

Barclay, A. H., and D. R. Toomey (2003), Shear wave splitting and crustal anisotropy at the Mid-Atlantic Ridge, 35°N, *J. Geophys. Res.*, *108*(B8), 2378, doi:10.1029/2001JB000918.

Barclay, A. H., D. R. Toomey, and S. C. Solomon (1998), Seismic structure and crustal magmatism at the Mid-Atlantic Ridge, 35°N, *J. Geophys. Res.*, *103*, 17,827–17,844.

Barclay, A. H., D. R. Toomey, and S. C. Solomon (2001), Microearthquake characteristics and crustal V_P/V_S structure at the Mid-Atlantic Ridge, 35°N, *J. Geophys. Res.*, *106*, 2017–2034.

Carbotte, S. M., et al. (2002), A multi-channel seismic investigation of ridge crest and ridge flank structure along the Juan de Fuca Ridge, *Eos Trans. AGU*, *83*(47), Fall Meet. Suppl., Abstract T72C-07.

Carlson, R. L. (1998), Seismic velocities in the uppermost oceanic crust: Age dependence and the fate of layer 2A, *J. Geophys. Res.*, *103*, 7069–7077.

Christeson, G. L., G. M. Kent, G. M. Purdy, and R. S. Detrick (1996), Extrusive thickness variability at the East Pacific Rise, 9°–10°N: Constraints from seismic techniques, *J. Geophys. Res.*, *101*, 2859–2873.

Collier, J. S., and S. C. Singh (1998), Poisson's ratio structure of young oceanic crust, *J. Geophys. Res.*, *103*, 20,981–20,996.

Crampin, S. (1993), A review of the effects of crack geometry on wave propagation through aligned cracks, *Can. J. Explor. Geophys.*, *29*, 3–17.

Cudrak, C. F., and R. M. Clowes (1993), Crustal structure of the Endeavour Ridge segment, Juan de Fuca Ridge, from a detailed seismic refraction survey, *J. Geophys. Res.*, *98*, 6329–6349.

Delaney, J. R., et al. (1991), JASON/ALVIN operations on the Endeavour segment, Juan de Fuca Ridge: Summer 1991, *Eos Trans. AGU*, *72*, Fall Meet. Suppl., F231.

Delaney, J. R., V. Robigou, R. E. McDuff, and M. K. Tivey (1992), Geology of a vigorous hydrothermal system on the Endeavour segment, Juan de Fuca Ridge, *J. Geophys. Res.*, *97*, 19,663–19,682.

Detrick, R. S., A. J. Harding, G. M. Kent, J. A. Orcutt, J. C. Mutter, and P. Buhl (1993), Seismic structure of the southern East Pacific Rise, *Science*, *259*, 499–503.

Detrick, R. S., S. Carbotte, E. V. Ark, J. P. Canales, G. Kent, A. Harding, J. Diebold, and M. Nedimovic (2002), New multichannel seismic constraints on the crustal structure of the Endeavour segment, Juan de Fuca Ridge: Evidence for a crustal magma chamber, *Eos Trans. AGU*, *83*(47), Fall Meet. Suppl., Abstract T12B-1316.

Dunn, R. A., and D. R. Toomey (1997), Seismological evidence for three-dimensional melt migration beneath the East Pacific Rise, *Nature*, *388*, 259–262.

Dunn, R. A., and D. R. Toomey (2001), Crack-induced seismic anisotropy in the oceanic crust across the East Pacific Rise (9°30′N), *Earth Planet Sci. Lett.*, *189*, 9–17.

Dziak, R. P., and C. G. Fox (1995), Juan de Fuca Ridge T-wave earthquakes August 1991 to present: Volcanic and tectonic implications, *Eos Trans. AGU*, *76*, Fall Meet. Suppl., F411.

Grevemeyer, I., and W. Weigel (1996), Seismic velocities of the uppermost igneous crust versus age, *Geophys. J. Int.*, *124*, 631–635.

Grevemeyer, I., and W. Weigel (1997), Increase of seismic velocities in upper oceanic crust: The "superfast" spreading East Pacific Rise at 14°14′S, *Geophys. Res. Lett*, *24*, 217–220.

Harding, A. J., G. M. Kent, and J. A. Orcutt (1993), A multichannel seismic investigation of upper crustal structure at 9°N on the East Pacific Rise: Implications for crustal accretion, *J. Geophys. Res.*, *98*, 13,925–13,944.

Hildebrand, J. A., M. A. Mcdonald, and S. C. Webb (1997), Microearthquakes at intermediate spreading-rate ridges: The Cleft segment megaplume on the Juan de Fuca Ridge, *Bull. Seismol. Soc. Am.*, *87*, 684–691.

Hooft, E. E. E., H. Schouten, and R. S. Detrick (1996), Constraining crustal emplacement processes from the variation on seismic layer 2A thickness at the East Pacific Rise, *Earth Planet. Sci. Lett.*, *142*, 289–309.

Houtz, R., and J. Ewing (1976), Upper crustal structure as a function of plate age, *J. Geophys. Res.*, *81*, 2490–2498.

Hussenoeder, S. A., R. S. Detrick, G. M. Kent, H. Schouten, and A. J. Harding (2002), Fine-scale seismic structure of young upper crust at 17°20′S on the fast spreading East Pacific Rise, *J. Geophys. Res.*, *107*(B8), 2158, doi:10.1029/2001JB001688.

Jacobson, R. S. (1992), The impact of crustal evolution on changes of the seismic properties of the uppermost ocean crust, *Rev. Geophys.*, *30*, 23–42.

Kappel, E. S., and W. B. F. Ryan (1986), Volcanic episodicity on a non-steady state rift valley along northeast Pacific spreading centers: Evidence from Sea MARC I, *J. Geophys. Res.*, *91*, 13,925–13,940.

Karsten, J. L., S. R. Hammond, E. E. Davis, and R. G. Currie (1986), Detailed geomorphology and neotectonics of the Endeavour segment, Juan de Fuca Ridge: New results from Seabeam swath mapping, *Geol. Soc. Am. Bull.*, *97*, 213–221.

Karsten, J. L., J. R. Delaney, J. M. Rhodes, and R. A. Liias (1990), Spatial and temporal evolution of magmatic systems beneath the Endeavour segment, Juan de Fuca Ridge: Tectonic and petrologic constraints, *J. Geophys. Res.*, *95*, 19,235–19,256.

Kelley, D. S., J. R. Delaney, and D. R. Yoerger (2001), Geology and venting characteristics of the Mothra hydrothermal field, Endeavour Segment, Juan de Fuca Ridge, *Geology*, *29*, 959–962.

Klein, F. W. (1978), Hypocenter location program HYPOINVERSE, 1, User's guide to versions 1, 2, 3, 4, in *U.S. Geol. Surv. Open File Rep.*, *78–694*, 103 pp.

Kong, L. S. L. (1990), Variations in structure and tectonics along the Mid-Atlantic Ridge, 23°N and 26°N, Ph.D. thesis, Woods Hole Oceanogr. Inst./Mass. Inst. of Technol. Joint Program, Woods Hole, Mass.

Lilley, M. D., M. C. Landsteiner, E. A. McLaughlin, C. B. Parker, A. S. M. Cherkaoui, G. Lebon, S. R. Veirs, and J. R. Delaney (1995), Real-time mapping of hydrothermal plumes on the Endeavor Segment of the Juan de Fuca, *Eos Trans. AGU*, *76*(46), Fall Meet. Suppl., F420.

Magde, L. S., A. H. Barclay, D. R. Toomey, R. S. Detrick, and J. A. Collins (2000), Crustal magma plumbing within a segment of the Mid-Atlantic Ridge, 35°N, *Earth Planet. Sci. Lett.*, *175*, 55–67.

McClain, J. S., M. L. Begnaud, M. A. Wright, J. Fondrk, and G. K. Von Damm (1993), Seismicity and tremor in a submarine hydrothermal field: The northern Juan de Fuca Ridge, *Geophys. Res. Lett.*, *20*, 1883–1886.

Moser, T. J. (1991), Shortest path calculation of seismic rays, *Geophysics*, *56*, 59–67.

Paige, C. C., and M. A. Saunders (1982), LSQR: An algorithm for sparse linear equations and sparse least squares, *ACM Trans. Math. Software*, *8*, 43–71.

Riedesel, M., J. A. Orcutt, K. C. Macdonald, and J. S. McClain (1982), Microearthquakes in the black smoker hydrothermal vent field, East Pacific Rise at 21°N, *J. Geophys. Res.*, *87*, 10,613–10,623.

Robigou, V., J. R. Delaney, and D. S. Stakes (1993), Large massive sulfide deposits in a newly discovered active hydrothermal system, the High-Rise field, Endeavour segment, Juan de Fuca Ridge, *Geophys. Res. Lett.*, *20*, 1887–1890.

Rohr, K. M. M. (1994), Increase of seismic velocities in upper oceanic crust and hydrothermal circulation on the Juan de Fuca plate, *Geophys. Res. Lett.*, *21*, 2163–2166.

Rohr, K. M. M., B. Milkereit, and C. J. Yorath (1988), Asymmetric deep crustal structure across the Juan de Fuca Ridge, *Geology*, *16*, 533–537.

Shaw, P. R. (1994), Age variations of oceanic crust Poisson's ratio: Inversion and a porosity evolution model, *J. Geophys. Res.*, *99*, 3057–3066.

Shearer, P. M. (1988), Cracked media, Poisson's ratio and the structure of the upper oceanic crust, *Geophys. J.*, *92*, 357–362.

Shearer, P. M., and J. Orcutt (1985), Anisotropy in the oceanic lithosphere-Theory and observations from the Ngendei seismic refraction experiment in the south-west Pacific, *Geophys. J. R. Astron. Soc.*, *80*, 493–526.

Shearer, P. M., and J. A. Orcutt (1986), Compressional and shear wave anistropy in the oceanic lithosphere- the Ngendei seismic refraction experiment, *Geophys. J. R. Astron. Soc.*, *87*, 967–1003.

Smith, D. K., and J. R. Cann (1992), The role of seamount volcanism in crustal construction at the Mid-Atlantic Ridge (24°–30°N), *J. Geophys. Res.*, *97*, 1645–1658.

Sohn, R. A., S. C. Webb, J. A. Hildebrand, and B. D. Cornuelle (1997), Three-dimensional tomographic velocity structure of upper crust, CoAxial segment, Juan de Fuca Ridge: Implications for on-axis evolution and hydrothermal circulation, *J. Geophys. Res.*, *102*, 17,679–17,698.

Stephen, R. A. (1985), Seismic anisotropy in the upper oceanic crust, *J. Geophys. Res.*, *90*, 11,383–11,396.

Tivey, M. K., and J. R. Delaney (1986), Growth of large sulfide structures on the Endeavour segment of the Juan de Fuca Ridge, *Earth Planet. Sci. Lett.*, *77*, 303–317.

Toomey, D. R., S. C. Solomon, G. M. Purdy, and M. H. Murray (1985), Microearthquakes beneath the median valley of the Mid-Atlantic Ridge near 23°N: Hypocenters and focal mechanisms, *J. Geophys. Res.*, *90*, 5443–5458.

Toomey, D. R., S. C. Solomon, and G. M. Purdy (1988), Microearthquakes beneath the median valley of the Mid-Atlantic Ridge near 23°N: Tomography and tectonics, *J. Geophys. Res.*, *93*, 9093–9112.

Toomey, D. R., G. M. Purdy, S. C. Solomon, and W. S. D. Wilcock (1990), The three-dimensional seismic velocity structure of the East Pacific Rise near latitude 9°30′N, *Nature*, *347*, 639–654.

Toomey, D. R., S. C. Solomon, and G. M. Purdy (1994), Tomographic imaging of the shallow crustal structure of the East Pacific Rise at 9°30′N, *J. Geophys. Res.*, *99*, 24,135–24,157.

Van Ark, E., R. Detrick, P. Canales, S. Carbotte, J. Diebold, M. Nedimovic, G. Kent, A. Harding, and W. Wilcock (2003), Seismic structure of the Endeavour segment, Juan de Fuca Ridge: Correlations of crustal magma chamber properties with seismicity, faulting, and hydrothermal activity, *Eos Trans. AGU*, *84*(46), Fall Meet. Suppl., Abstract B12A-0752.

White, D. J., and R. M. Clowes (1990), Shallow crustal structure beneath the Juan de Fuca Ridge from 2-D seismic refraction tomography, *Geophys. J. Int.*, *100*, 349–367.

White, D. J., and R. M. Clowes (1994), Seismic attenuation structure beneath the Juan de Fuca Ridge from tomographic inversion of amplitudes, *J. Geophys. Res.*, *99*, 3043–3056.

White, R. S., and R. B. Whitmarsh (1984), An investigation of seismic anisotropy due to cracks in the upper oceanic crust at 45°N, Mid-Atlantic Ridge, *Geophys. J. R. Astron. Soc.*, *79*, 439–467.

Wilcock, W. S. D. (2001), Tidal triggering of microearthquakes on the Juan de Fuca Ridge, *Geophys. Res. Lett*, *28*, 3999–4002.

Wilcock, W. S. D., and J. R. Delaney (1996), Mid-ocean ridge sulfide deposits: Evidence for heat extraction from magma chambers or cracking fronts?, *Earth Planet. Sci. Lett.*, *145*, 49–64.

Wilcock, W. S. D., S. D. Archer, and G. M. Purdy (2002), Microearthquakes on the Endeavour segment of the Juan de Fuca Ridge, *J. Geophys. Res.*, *107*(B12), 2336, doi:10.1029/2001JB000505.